International Journal of Minerals, Metallurgy and Materials
Accepted manuscript, https://doi.org/10.1007/s12613-025-3334-0

Novel insights into the synergistic depression mechanism of H_2O_2 and Fe^{3+} on pyrite in low-alkalinity Cu–S flotation separation

Yubin Sun[1], *Qian Zhang*[1),✉], *Shuming Wen*[1,2),✉], *Yongchao Miao*[1)], *and Ping Zhang*[1)]

1) State Key Laboratory of Complex Nonferrous Metal Resources Clean Utilization, Faculty of Land Resource Engineering, Kunming University of Science and Technology, Kunming 650093, China

2) Southwest United Graduate School, Kunming, Yunnan 650092, China

✉Corresponding authors: Qian Zhang E-mail: zqian9865@163.com; Shuming Wen E-mail: shmwen@126.com

Abstract: Conventional lime depressants used in copper sulphide flotation separation are constrained by the persistent challenges of scaling, corrosion and compromised target metal recovery, necessitating the development of efficient and green alternatives. This study demonstrates the synergistic depression of pyrite by H_2O_2/Fe^{3+} under low-alkalinity conditions. The complementary action pathways were systematically elucidated by multi-scale characterisation techniques including mono- and mixed- mineral flotation tests, surface and solution analysis. Flotation test results demonstrate that the combined depressant H_2O_2/Fe^{3+} enables efficient separation of chalcopyrite and pyrite. Under the optimal mixed minerals separation conditions of 0.025vol% H_2O_2 and 2×10^{-5} mol/L Fe^{3+}, the artificial mixed minerals flotation test yielded a copper concentrate with a chalcopyrite grade of 30.51wt%, while the chalcopyrite recovery was stably maintained above 88%. Investigations into the depression mechanism and surface hydrophobicity reveal that H_2O_2 selectively

oxidises disulphide (S_2^{2-}) to sulphate (SO_4^{2-}) while facilitating Fe^{2+} conversion to Fe^{3+}, generating hydrophilic Fe-SO_4/Fe-OOH/$Fe(OH)_3$ coatings that disrupt the surface natural hydrophobicity. Simultaneously, Fe^{3+} hydrolytic to the hydroxyl complexes ($Fe(OH)_2^+$and $Fe(OH)_3$), its electrostatically adsorb and chemically bond to H_2O_2-oxidised pyrite surfaces and forming dense hydrophilic layers. The faster oxidation of pyrite originates from its fundamental structural properties, specifically its high surface electronic activity and relatively weak Fe–S bonds, which collectively render it more susceptible to attack by H_2O_2，unlike chalcopyrite with its stable lattice and strong covalent Cu–S bonds. Consequently, the robust covalent Cu–S bonds of chalcopyrite effectively resist oxidation, while its limited Fe^{3+} adsorption capacity favors the adsorption of sodium ethyl xanthate (SEX) at copper-active sites. As a result, the H_2O_2/Fe^{3+} system exerts only minimal depression on chalcopyrite, thereby providing a sound theoretical basis and a practical technical strategy for the selective separation of copper-sulfide ores. Furthermore, the findings of this study contribute to the development of low-alkalinity, high-selectivity sulfide ore processing methods, demonstrating considerable potential for industrial application.

Keywords: Chalcopyrite; Pyrite; Low alkalinity; Flotation separation; Depression mechanism

1. Introduction

Copper is a strategically indispensable metal for modern industrial infrastructure, advanced technologies and global economic security [1-2]. It is derived primarily

from chalcopyrite ($CuFeS_2$), the dominant copper sulphide mineral governing global resource extraction [3]. It frequently co-occurs with pyrite in sulphide deposits, necessitating effective separation for efficient chalcopyrite recovery [4-5]. Flotation remains the industrial benchmark for Cu–Fe sulphide separation, where depressants enhance pyrite hydrophilicity to achieve selective chalcopyrite enrichment [6]. Although lime (CaO) can achieve effective pyrite depression [7], its application poses remarkable operational challenges: Reaction with pulp CO_2 and sulphates generates insoluble $CaCO_3$ and $CaSO_4$ scales, respectively, which foul pipelines, pumps and flotation cells, impairing efficiency and escalating maintenance. The concomitant high alkalinity accelerates the corrosion of metallic equipment, thereby reducing service lifetimes [8-9]. Notably, excessive lime suppresses target metal recovery, compromising the extraction of copper and precious metals [10]. Consequently, contemporary depressant research prioritises environmental compatibility, efficiency and selectivity to address inherent constraints of conventional toxic or low-selectivity reagents in complex ore processing [11-13]. Although organic alternatives (polysaccharides, chelators and plant extracts) have garnered interest owing to their eco-friendliness and abundance, they are limited by their performance instability under fluctuating conditions, high dosage requirements and marginal economics [14-15]. While inorganic depressants maintain industrial prevalence owing to their cost-effectiveness and technological maturity, their toxicity, selectivity deficits and environmental incompatibilities demand urgent resolution. Thus, the development of

high-performance, eco-compatible pyrite depressants constitutes a critical pathway towards sustainable polymetallic sulphide mineral processing [16-17].

Flotation fundamentally relies on the selective adhesion of target minerals to bubbles, governed by surface hydrophobicity modulation. In this process, the pulp system comprises a complex multi-phase suspension typically containing dissolved metal ions originating from mineral dissolution and fluid inclusion release [18]. These metal ions critically influence flotation performance through their multi-faceted effects on pulp conditioning, reagent adsorption, bubble mineralisation and froth separation [19]. Therefore, a comprehensive understanding of ion sources, speciation, interfacial interactions and complex interplay with minerals, reagents and solution environments is imperative for efficient resource utilisation. Metal ions predominantly affect flotation through mineral activation, depression, reagent adsorption modulation and bubble property alteration [20]. As an effective metallic mineral depressant, Fe^{3+} has been extensively investigated, research results demonstrated that Fe^{3+} suppresses smithsonite floatability by generating surface Fe-OOH species that impede active sulphide formation [21]. Besides, Li et al. revealed that while Fe^{3+} depresses arsenopyrite via chemisorption, redox reactions, and hydrophilic precipitation, its efficacy is concentration-dependent. The use of excessive Fe^{3+} risks disrupting pulp equilibrium and forming non-selective precipitates, which can compromise the recovery of target metals [22]. Collectively, these studies confirm the efficacy of Fe^{3+} as a flotation depressant for mineral separation. However, given the inherent

limitations of single-component Fe^{3+} depression, synergistic depression systems combining Fe^{3+} with auxiliary reagents have become an emerging research frontier. He et al. confirmed that combining Fe^{3+}/Cu^{2+}/Al^{3+} with sodium silicate forms dense metal–silicate hydrophilic layers on quartz in oleate systems, achieving >90% quartz depression with minimal fluorite depression and thereby enhancing fluorite–quartz separation efficiency [23]. Similarly, Dong et al. demonstrated that Fe^{3+}–NH_4^+ synergy selectively depresses chalcopyrite through NH_4^+-enhanced Fe^{3+} adsorption to form hydrophilic composite layers while minimally affecting arsenopyrite. This synergistic effect considerably enhances the separation selectivity of chalcopyrite from arsenopyrite [24].

Oxidation technology is an effective surface modification strategy for sulphide ore flotation separation. Preliminary studies have reported synergistic depression between the oxidants and metal ions. Ding et al. demonstrated that the H_2O_2/Fe^{2+} system achieves oriented pyrite surface hydrophilisation and depression via Fenton reactions, confirmed the synergistic depressant effect of oxidant and metal ions on minerals. However, critical knowledge gaps remain: (i) sufficient systematic analysis of interactions between oxidation modification processes and metal ion adsorption behaviour is still lacking, and (ii) the performance benchmarking against single depressants is inadequate. Furthermore, the persistent challenge of high Fe^{2+} dosage severely constrains industrial implementation [25]. Therefore, this study develops an innovative synergistic system using H_2O_2 as an oxidant and Fe^{3+} as a depressant to

enable low-alkalinity chalcopyrite–pyrite separation. The impact of the reagent on mineral recovery is quantified via flotation tests, while the synergistic depression mechanism of H_2O_2/Fe^{3+} on pyrite is deciphered through multimodal characterisation: interfacial properties (zeta potential/contact angle), elemental speciation—Inductively Coupled Plasma Optical Emission Spectrometer (ICP-OES), surface chemistry—X-ray Photoelectron Spectroscopy (XPS), Fourier transform infrared (FTIR), Raman and Time of Flight Secondary Ion Mass Spectrometry (ToF-SIMS); microtopography—Scanning Electron Microscopy and Energy Dispersive Spectrometer (SEM—EDS) and Atomic force microscopy (AFM); local electrochemistry—Localised electrochemical impedance spectroscopy (LEIS).

2. Experimental

2.1. Materials and reagents

Assay-grade pyrite and chalcopyrite specimens were procured from Jiangxi Province. The as-received specimens were subjected to sequential processing: crushing, hand-picking, grinding and sieving to obtain specific size fractions. Prior to testing, all mineral samples were stored in vacuum desiccators to prevent oxidation. Atomic absorption spectrometry confirmed >95% purity for both minerals. The size-classified samples were allocated as follows: −74 + 38 μm fraction: micro-flotation tests, surface dissolution analysis and SEM–EDS; −38 μm fraction: XPS/ ToF-SIMS/ FTIR /AFM and contact angle measurements.

Conventional flotation reagents were utilised: SEX (collector), methyl isobutyl

carbinol (MIBC, frother), HCl and NaOH for pH regulation, H_2O_2 (depressant), and $FeCl_3 \cdot 6H_2O$. All procured from Shanghai Xilong Chemical Co., Ltd. XRD analysis did not detect any impurity phases, indicating that both chalcopyrite and pyrite are predominantly pure mineral phases without interference from other phases.

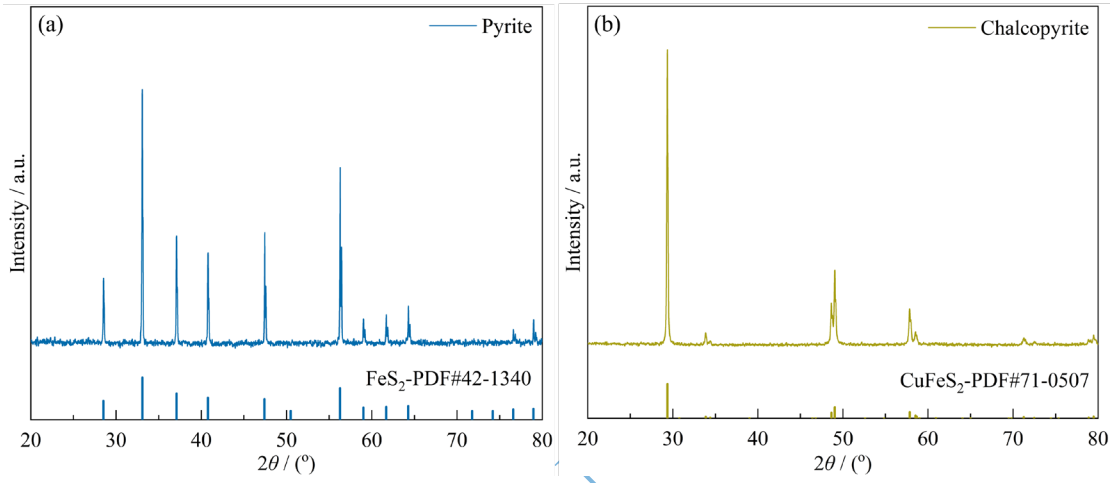

Fig. 1. X-ray diffraction patterns of pyrite (a) and chalcopyrite (b).

2.2. Flotation test

Micro-flotation tests employed an XFGC II unit (Jilin Exploration Machinery) at 1602 rpm, with a gas flow rate set at 0.25 m^3 /h. For single minerals: 2-g ultrasonicated chalcopyrite/pyrite samples (3 min oxide removal; 2 min settling) were transferred to 40-mL cells with 38 mL deionised water. Pre-flotation H_2O_2/Fe^{3+} addition preceded pH adjustment (NaOH/HCl) and 3-min conditioning. Frother introduction (1 min agitation) initiated 3-min aeration/froth collection. Products were filtered, dried, and weighed for recovery calculation. Mixed-mineral tests used identical protocols with 1:1 chalcopyrite-pyrite feed. Concentrates/tailings were chemically assayed to determine mineral-specific recoveries. Triplicate tests yielded

mean-reported results.

2.3. Zeta potential measurement

Mineral specimens (−38 μm) were pulverised to −5 μm via planetary ball milling (MM400). Exactly 0.05 g of the pulverised material was added to 40 mL of a 5×10^{-3} mol/L KCl suspension medium, which functioned as an inert supporting electrolyte to stabilize the system's ionic strength and prevent interference with the intrinsic surface charge of the minerals. Following ultrasonic dispersion to ensure a homogeneous suspension, depressants and collectors were sequentially introduced under predetermined conditions. The mixture reacted for 5 min after depressant addition; thereafter, the collector was introduced, and the reaction proceeded for 3 min. The solution pH was continuously maintained within the target range throughout these conditioning stages. Upon completion of the reaction, the contents of the beaker were subjected to sedimentation for facilitating phase separation. A measured aliquot of the upper suspension was then extracted and immediately transferred to a zeta potential analyser (NanoZS90) for measurement. Measurements were performed in triplicate for each sample, with the mean values reported as the final results. Additionally, Fe^{3+} speciation distribution across the experimental pH range was computationally determined using Visual MINTEQ 3.1 software.

2.4. ICP–OES measurement

Precisely 2 g of the mineral samples (particle size: 38–74 μm) were ultrasonically cleaned in deionised water to remove surface impurities.

Post-sedimentation, the supernatant was discarded. Minerals were then transferred to new containers with 40 mL deionised water and homogenised by magnetic stirring. The solution pH was adjusted to the experimental target via reagent addition, and the reaction proceeded for 5 min. The mixture was filtered; the filtrate centrifuged at 2500 rpm for 15 min. A defined supernatant aliquot underwent ICP-OES analysis for metal concentration determination. Triplicate testing was conducted under identical conditions to ensure reproducibility, and the mean values were reported. Ion adsorption on the mineral surface was quantified through the concentration changes in the pulp solution, using Eq. (1) for calculation.

$$\Delta C = C_0 - C \quad (1)$$

where C_0 denotes the initial ion concentration ($mol \cdot L^{-1}$) and C represents the supernatant concentration after the reaction.

2.5. FTIR and Raman spectroscopy measurements

Ultrasonicated mineral samples (2 g; −38 μm) were dispersed in 40 mL deionised water under magnetic stirring. Depressants were introduced concurrently with pH adjustment using NaOH or HCl solutions; this was followed by a 10-min reaction period. The resultant slurry was vacuum-filtered, and the collected solids were rinsed thrice with deionised water prior to vacuum drying (0.08 MPa, 25°C). For spectroscopic analysis, dried samples were homogenised with KBr powder in a 1:100

mass ratio, pressed into pellets and lamp-dried to evaporate the residual solvents. The pellet-mounted specimens were examined via FTIR spectroscopy (Tensor 27) and Raman spectroscopy (LabRam HR Evolution). The acquired spectra were processed using dedicated software (OMNIC for FTIR; LabSpec6 for Raman).

2.6. XPS analysis

XPS analysis was conducted on a PHI 5000 spectrometer (ULVAC-PHI, Chigasaki, Japan) to determine the surface elemental compositions. Specimen preparation mirrored the micro-flotation test protocols: post-reaction samples were vacuum-dried isothermally at 40°C before analysis, a condition established in published literature to effectively remove moisture without altering the adsorbed collector species [26]. This characterisation elucidated that H_2O_2/Fe^{3+} induced modifications of the elemental states and surface chemistries of pyrite and chalcopyrite. The acquired spectra were processed using Multipak software (PHI) to perform peak deconvolution of full-survey scans and high-resolution elemental spectra. The metallic element spectra employed asymmetric peak functions, while non-metallic elements utilised Gaussian–Lorentzian mixed functions for optimal fitting.

2.7. ToF-SIMS analysis

The ToF-SIMS analysis of pyrite was conducted using a ToF.SIMS-5 instrument (ION-TOF GmbH, Germany). Specimen preparation followed protocols identical to

the XPS measurements. The analytical parameters included Bi^{3+} primary ion source (30 keV energy and 10 kHz pulse frequency) and an analysis area of 500 × 500 μm; positive or negative ion spectra were acquired simultaneously. The characteristic ions—OH^-, FeO_2^-, S^-, S_2^{2-}, SO_4^{2-}, SO_2^{2-}, Fe^+ and Fe_2S^+, were specifically targeted. Secondary ion distribution maps and signal intensities were processed and quantified using the manufacturer-supplied SurfaceLab software.

2.8. LEIS measurement

A mineral slice was conductively bonded to a wire on one side, epoxy-encapsulated as the working electrode. The opposite face was mirror-polished. LEIS measurements employed a Versa SCAN micro-electrochemical workstation (AMETEK Inc.) with 10^{-3} mol/L KCl electrolyte and Ag/AgCl reference. Parameters: 1000×1000 μm scan range, 50 μm step size, 1 kHz frequency, 10 mV bias. Precision electrode fabrication and parameterization ensured micro-domain electrochemical measurement fidelity.

2.9. AFM analysis and contact angle measurement

AFM was performed using a Dimension ICON instrument (Bruker, USA) to quantify reagent-induced mineral surface roughness alterations. Specimens were mirror-polished to sub-nanometre root-mean-square roughness before testing. The treated sheets were subjected to 20-min reagent exposure and subsequently to ambient desiccation for stabilising the surfaces for AFM characterisation. Specimen preparation protocols identical to those for the contact angle measurements were

employed. A JY-82A goniometer (Chengde Dingsheng Testing Machine Co., China) was used to determine the surface hydrophobic or hydrophilic properties.

2.10. SEM–EDS analysis

H_2O_2/Fe^{3+} treatments modified pyritic surface morphology and composition. These alterations were characterised by SEM–EDS performed using a ZEISS Sigma 300 apparatus (Oberkochen, Germany). For the measurements, SEM-EDS employed an SE2 detector at 3 kV (morphology) and 15 kV (elemental mapping). Mineral samples (2 g) underwent ultrasonic cleaning per flotation protocols. Supernatants were decanted post-sedimentation; residues transferred to flotation cells with 50 mL deionised water. The target reagent concentrations were introduced and homogenised. The reacted minerals were vacuum-filtered, dried (−0.08 MPa, 40°C) and analysed. The qualitative and semiquantitative characterisations of surface microstructures and elemental distributions were realised through controlled experimental parameterisation.

3. Results and Discussion

3.1. Micro-flotation test

3.1.1 Single-mineral micro-flotation tests

First, the flotation behaviour of pyrite and chalcopyrite was evaluated as a function of the collector SEX concentration at pH 8.0 (Fig. 2a). The recovery of both minerals increased with increasing SEX concentration, stabilising at 90.14% for pyrite and 92.50% for chalcopyrite when the concentration reached 1.5×10^{-4} mol/L. This

demonstrates the effective collection of both minerals by SEX, hindering their selective separation. Subsequently, at fixed SEX (1.5×10^{-4} mol/L), H_2O_2 concentration effects on mineral recovery were assessed (Fig. 2b). Increasing H_2O_2 concentration hindered the recovery of both minerals. Notably, at 0.025vol% H_2O_2, pyrite recovery considerably dropped to 72.03%, while chalcopyrite recovery remained high at 95.83%. Further increasing H_2O_2 to 0.05vol% reduced the chalcopyrite recovery to 88.30%, indicating that excessive H_2O_2 also depresses chalcopyrite [27]. Therefore, to minimise chalcopyrite depression, 0.025vol% H_2O_2 was used in subsequent tests. Thereafter, the effect of Fe^{3+} on mineral recovery was examined for SEX and H_2O_2 concentrations of 1.5×10^{-4} mol/L and 0.025vol%, respectively (Fig. 2c). Increasing Fe^{3+} concentration alone (1×10^{-5} to 1×10^{-4} mol/L) moderately depressed pyrite, yet its recovery exceeded 20%, indicating insufficient depression efficiency. Crucially, H_2O_2 pretreatment significantly intensified Fe^{3+}-induced pyrite depression, lowering the threshold Fe^{3+} dosage. At 2×10^{-5} mol/L Fe^{3+} (following H_2O_2 pre-treatment), pyrite recovery plunged to 5.11%. Importantly, chalcopyrite recovery remained above 91% within the Fe^{3+} concentration range of 0–8×10^{-5} mol/L, demonstrating excellent selectivity. Finally, the flotation of individual minerals was examined across pH 4–12 under optimised reagent conditions (SEX: 1.5×10^{-4} mol/L, H_2O_2: 0.025vol%, Fe^{3+}: 2×10^{-5} mol/L; Fig. 2d). Chalcopyrite recovery consistently exceeded 90% throughout the pH range. Conversely, pyrite recovery declined at elevated pH, falling below 6% at pH ≥ 8.

These single-mineral micro-flotation results confirmed the effective depression of pyrite by the H_2O_2/Fe^{3+} system. Subsequently, the system was validated via artificial mixed minerals (chalcopyrite–pyrite) separation tests.

3.1.2 Artificial mixed mineral micro-flotation tests

Following positive mono-mineral flotation outcomes, mixed-mineral tests were performed. Fig. 2(e) demonstrates Fe^{3+} and H_2O_2 concentration effects on selective separation at pH 8.0 with 1×10^{-4} mol/L SEX. Evaluation of H_2O_2 concentration (0.00625–0.05vol%) revealed satisfactory separation performance at 0.025vol%, the copper concentrate assayed 30.67wt% Cu at 88.26% recovery. Although a marginally higher grade (31.40wt%) was obtained at 0.05vol% H_2O_2, its recovery decreased to 87.84%. Subsequently, with H_2O_2 fixed at 0.025vol%, Fe^{3+} concentrations (1.5×10^{-5} and 2.5×10^{-5} mol/L) were evaluated. Neither concentration yielded improved separation indices compared with the established 2×10^{-5} mol/L Fe^{3+} condition. Therefore, the optimal mixed minerals separation conditions were determined to be 0.025vol% of H_2O_2 and 2×10^{-5} mol/L of Fe^{3+}. The flotation performance under these optimal depressant concentrations was further assessed across pH 8–12 (Fig. 2f). Efficient separation was maintained at pH 8, 10 and 12, yielding copper concentrates with grades of 30.51wt%, 30.74wt% and 32.08wt%, respectively and recoveries of 88.30%, 85.46% and 83.90%, respectively. In summary, the synergistic H_2O_2/Fe^{3+} system facilitates efficient chalcopyrite-pyrite separation, offering a viable approach for complex copper sulphide ore beneficiation.

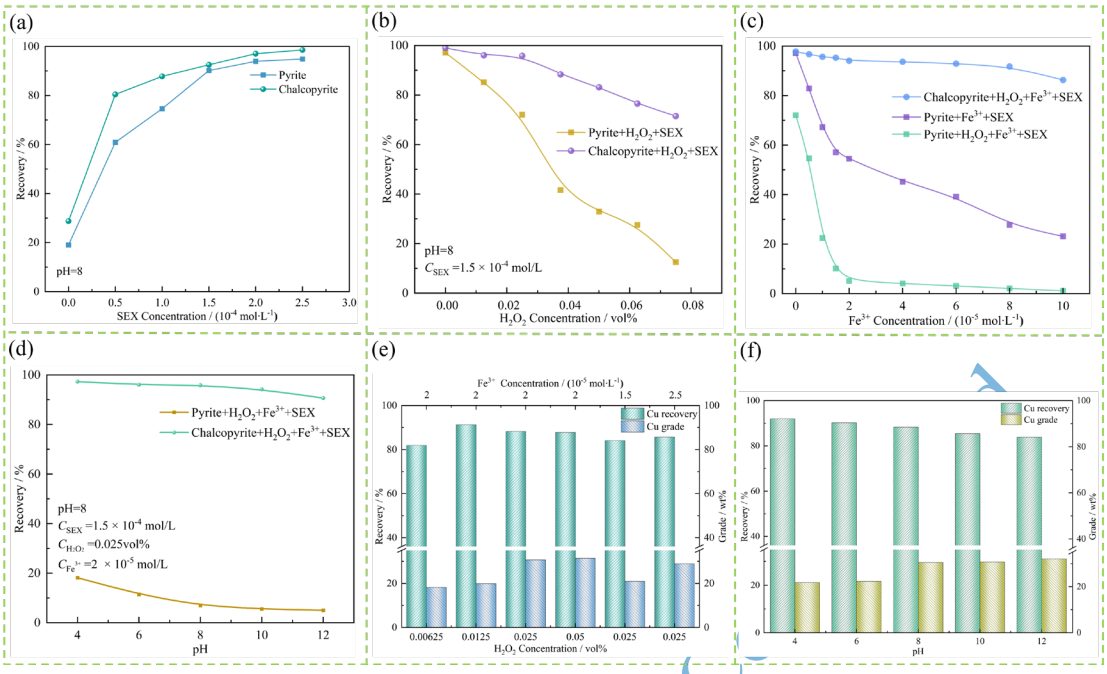

Fig. 2. Results of the single-mineral micro-flotation tests (a–d); results of the artificial mixed minerals micro-flotation tests (e, f).

3.2. H_2O_2/Fe^{3+} synergistic depression mechanisms at pyrite-chalcopyrite interfaces

3.2.1 Surface analysis of chalcopyrite-pyrite systems under varying reagent regimes

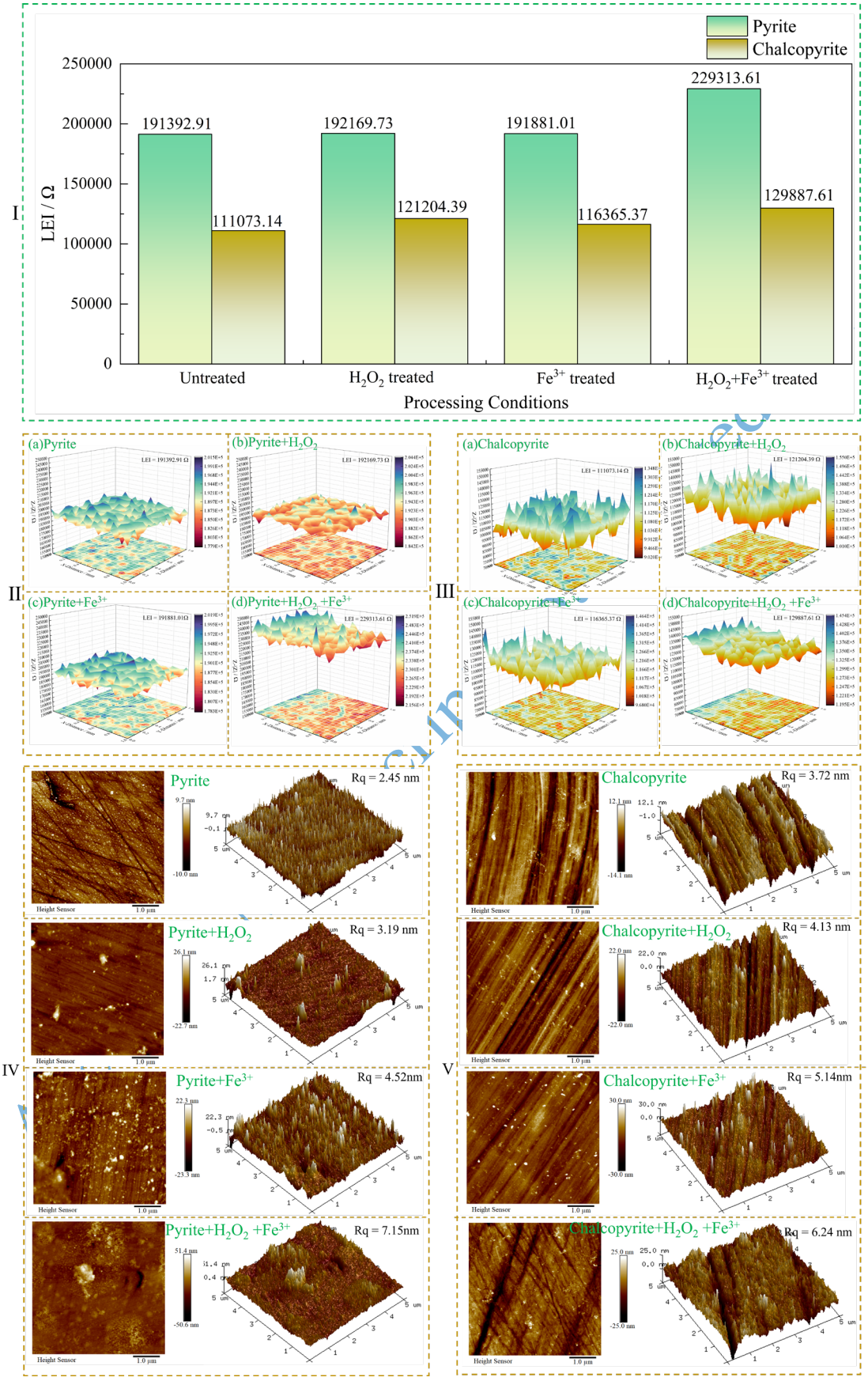

Fig. 3. (I) Impedance Comparison Bar Chart; LEIS results under different

conditions: (II) pyrite (III) chalcopyrite; AFM images treated under different conditions: (IV) pyrite (V) chalcopyrite.

In the field of mineral processing research, LEIS is mainly applied to characterise the electrochemical reaction processes on mineral surfaces for investigating key issues such as the oxidation of sulphide mineral surfaces, sulphidation of oxidised minerals, adsorption of flotation reagents, interactions between sulphide minerals and mechanisms of mineral chemical leaching [28]. Fig. 3 (I, II, III) depicts the LEIS spectra of pyrite under different reagent treatments, visually representing the distribution and variation of surface impedance through three-dimensional color mapping and bar charts. Untreated pyrite exhibited 191,392.91 Ω mean impedance; Fe^{3+} treatment marginally increased it to 191,881.01 Ω. Moreover, after treatment with H_2O_2 alone, the surface impedance of pyrite considerably increases to 192169.73 Ω, which is attributed to H_2O_2 oxidation that catalyzes surface ferric oxide species formation, consistent with existing research conclusions [29]. In contrast, after sequential treatment with H_2O_2 and Fe^{3+}, pyrite surface impedance surges, with an average value of 229313.61 Ω, an increase of 37920.69 Ω compared with the original ore sample. This substantial increase indicates that sequential treatment with H_2O_2 and Fe^{3+} leads to the formation of a more compact iron (oxy)hydroxide layer on the pyrite surface. Under the same treatment conditions, chalcopyrite shows a similar variation pattern (Fig. 3II). Untreated chalcopyrite exhibited 111,073.14 Ω mean impedance; sole Fe^{3+} or H_2O_2 treatment elevated values

to 116,365.37 Ω and 121,204.39 Ω respectively, respectively. After sequential treatment with H_2O_2 and Fe^{3+}, the surface impedance of chalcopyrite increases to 129887.61 Ω, an increase of 18814.47 Ω. Notably, this increase is considerably lower than that of pyrite under the synergistic treatment condition (differing by approximately one order of magnitude). The aforementioned results confirm that Fe^{3+} has selective adsorption characteristics on the pyrite surface, and H_2O_2 pre-treatment can generate specific oxides on the surface. This change in the surface properties leads to the formation of a high-impedance passive layer on the pyrite surface, depressing its floatability during the flotation process.

AFM characterisation (Fig. 3IV&V) revealed distinct surface topographies. Pristine pyrite exhibited densely packed spike-like structures (root mean square roughness, *R*q = 2.45 nm), whereas chalcopyrite displayed minor scratches (*R*q = 3.72 nm). Fe^{3+} treatment induced pyramidal protrusions atop the existing pyrite spikes (*R*q = 4.52 nm) with negligible morphological alteration on chalcopyrite. Furthermore, H_2O_2 treatment substantially modified the pyrite surfaces, flattening the spikes into sparse ridge-like features (pyrite: *R*q = 3.19 nm; chalcopyrite: *R*q = 4.13 nm). This transformation is attributed to the oxidative degradation of the hydrophobic sulphur species on pyrite (consistent with the XPS and ToF-SIMS data), with minimal impact on chalcopyrite. Sequential H_2O_2/Fe^{3+} treatment triggered drastic pyrite reorganisation into clustered protrusions (*R*q = 7.15 nm; final height: 0.4–51.4 nm; initial height: 0.1–9.7 nm). In contrast, chalcopyrite underwent modest changes (*R*q = 6.24 nm; final

height: 0–25 nm; initial height: 1–12.1 nm), indicating considerably stronger Fe^{3+} adsorption affinity on H_2O_2-modified pyrite surfaces than on chalcopyrite (supported by ICP–OES). Collectively, these morphological and topographical transformations demonstrate that sequential H_2O_2/Fe^{3+} treatment selectively restructures pyrite through complementary mechanisms: H_2O_2 degrades hydrophobic components, while Fe^{3+} consolidates hydrophilic complexes, enabling efficient depression.

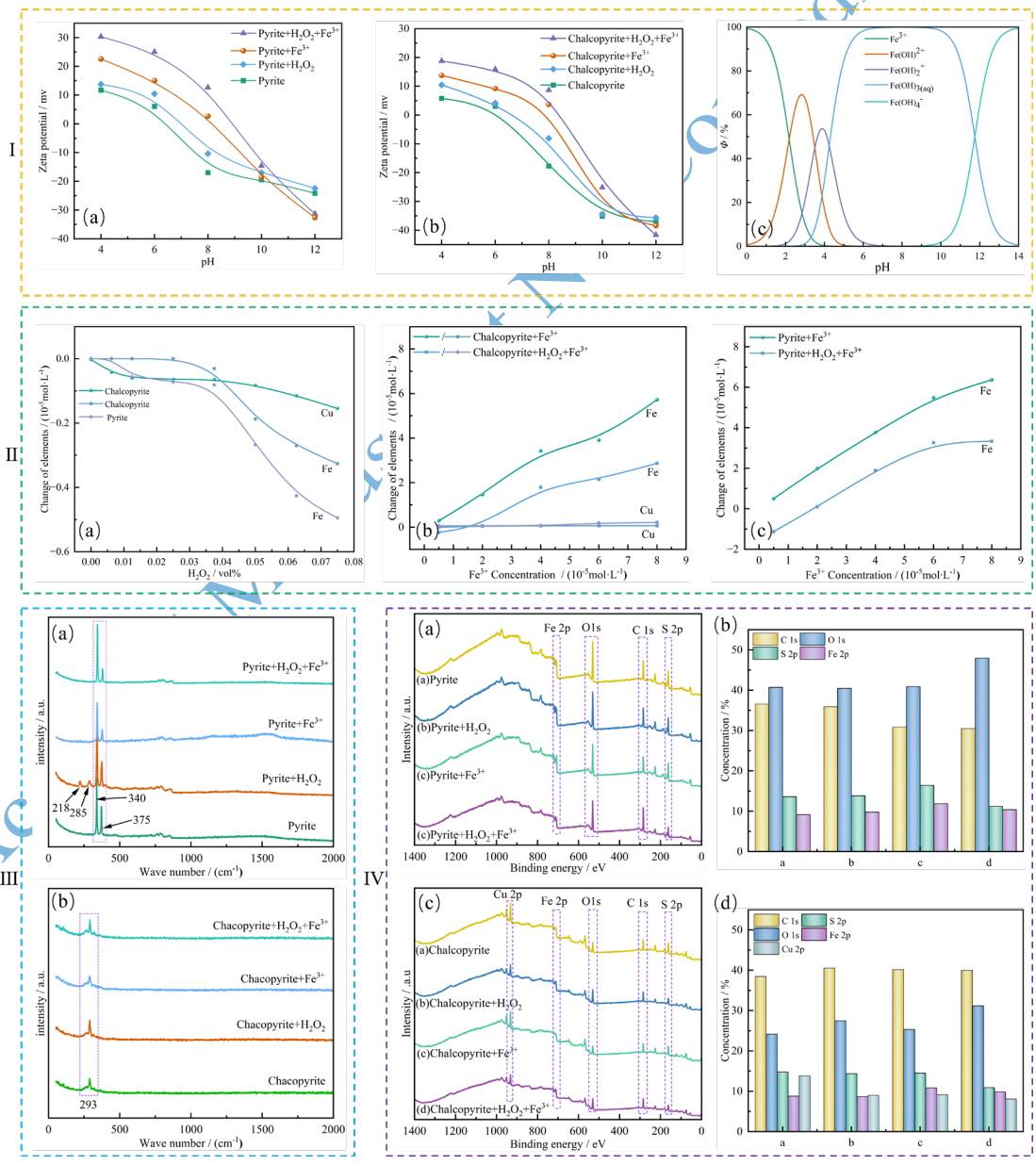

Fig. 4. I. Relationship between the potential and pH for (a) pyrite and (b)

chalcopyrite; Relationship between Fe^{3+} component percentage and pH (c); II. (a) Effect of H_2O_2 dosage on the surface element dissolution of chalcopyrite and pyrite; effects of H_2O_2 pre-treatment on the Fe^{3+} adsorption capacity of (b) chalcopyrite and pyrite (c); III. Raman spectra of (a) pyrite and (b) chalcopyrite; IV. XPS full spectra and atomic concentration analysis results of (a, b) pyrite and (c, d) chalcopyrite.

Zeta potential measurements assessed surface electrochemical evolution of chalcopyrite-pyrite under varying depressant regimes. These measurements, combined with solution chemistry calculations, allowed the analysis of the main existing species of Fe^{3+} that affect the surface electrical properties of minerals under different pH conditions. Fig.4I(a,b) shows reagent-free zeta potentials of both minerals declining with pH elevation, resulting from enhanced OH^- adsorption on surfaces at higher pH, considerably enhancing their electronegativity. Upon the sole action of H_2O_2, the surface zeta potentials of both minerals shift considerably to positive values because of the oxidation of hydrophobic disulphide (S_2^{2-}) on the mineral surfaces to hydrophilic sulphate (SO_4^{2-}) by H_2O_2, accompanied by the dissolution of iron ions to form hydroxylated surface species [30]. The zeta potential further increases when Fe^{3+} is added after pre-treatment with H_2O_2. Notably, H_2O_2/Fe^{3+} synergy enhanced pyrite zeta potential more pronouncedly than chalcopyrite. This indicates that oxidation by H_2O_2 and adsorption of Fe^{3+} are more likely to occur on the pyrite surface, which is consistent with previous research results [31]. Furthermore, at pH > 11, the zeta potential of pyrite treated with Fe^{3+} or

H_2O_2/Fe^{3+} is lower than that of the original (untreated) state. Similarly, a similar phenomenon was observed for chalcopyrite co-treated with H_2O_2 and Fe^{3+}. According to the solution chemistry calculation results shown in Fig.4I(c), Fe^{3+} is completely hydrolysed to $[Fe(OH)_4]^-$ (accounting for ≥98%) at pH > 11，under this condition, the negatively charged hydroxyl complexes bind to the M–OH groups (M = Fe, Cu) on the mineral surfaces through hydrogen bonds, causing a negative shift in potential.

The elemental leaching from pyrite and chalcopyrite surfaces under varying systems was quantified via ICP–OES. Fig. 4II(a) shows Fe and Cu dissolution profiles as a function of H_2O_2 concentration. Increasing H_2O_2 concentration promoted the gradual leaching of Fe and Cu from both minerals. Crucially, chalcopyrite exhibited a distinct inflection in Fe dissolution at 0.025vol% H_2O_2, Minimal Fe and Cu leaching occurred below this threshold, while Fe dissolution increased sharply above it. Cu dissolution underwent a delayed inflection at 0.04vol% H_2O_2, confirming that Fe was preferentially leached during chalcopyrite oxidation. The results of single-mineral flotation tests corroborated this threshold, with chalcopyrite recovery declining significantly below 0.025vol% H_2O_2. This correlation establishes that excessive H_2O_2 deteriorates floatability by dissolving the surface Fe and Cu atoms, thereby deactivating the collector adsorption sites. Consequently, stringent H_2O_2 concentration control is essential to preserve the chalcopyrite floatability. Paradoxically, Fig. 4II(b, c) demonstrate reduced Fe^{3+} adsorption on both minerals following H_2O_2 pre-treatment. This evidences that the synergistic H_2O_2/Fe^{3+} depression of pyrite does not originate

from enhanced Fe^{3+} adsorption.

Raman spectroscopy further elucidated the surface modifications of pyrite and chalcopyrite induced by H_2O_2/Fe^{3+} treatment. The chalcopyrite spectra (Fig. 4IIIb) exhibited a characteristic A_1g vibrational mode at 293 cm^{-1}, this mode is attributed to the symmetric stretching of $[S_2]^{2-}$ dimers [32]. Notably, no new peaks emerged upon H_2O_2/Fe^{3+} exposure. Conversely, the pyrite spectra (Fig. 4IIIa) revealed distinct vibrational signatures: an Eg mode at 340 cm^{-1} (Fe–S stretching) and Ag mode at 375 cm^{-1} ($[S_2]^{2-}$ symmetric stretch). H_2O_2 treatment resulted in new peaks at 218 and 285 cm^{-1}, assigned to polysulphide species (Sn^{2-}, n = 2–8) formation [33]. Crucially, subsequent Fe^{3+} application eliminated these features via signal shielding by the iron hydroxide overlayers [34]. These results demonstrate that H_2O_2 modifies pyrite surfaces through sulphur speciation transformation ($S_2^{2-} \rightarrow SO_4^{2-}$), while Fe^{3+} selectively adsorbs on the modified surfaces to form synergistic depression-enabling hydrophilic coatings.

Table 1. Relative atomic concentrations on pristine and treated Chalcopyrite surfaces.

Sample	Relative atomic concentration				
	C 1s	O 1s	S 2p	Fe 2p	Cu 2p
Chalcopyrite	38.46	24.17	14.76	8.79	13.82
Chalcopyrite+H_2O_2	40.53	27.47	14.35	8.69	8.96

Chalcopyrite+Fe^{3+}	40.14	25.33	14.51	10.85	9.17
Chalcopyrite+H_2O_2 +Fe^{3+}	40.01	31.19	10.91	9.83	8.06

Table 2. Relative atomic concentrations on pristine and treated Pyrite surfaces.

Sample	Relative atomic concentration			
	C 1s	O 1s	S 2p	Fe 2p
Pyrite	36.56	40.71	13.59	9.14
Pyrite+H_2O_2	35.92	40.46	13.83	9.79
Pyrite+Fe^{3+}	30.84	40.89	16.42	11.85
Pyrite+H_2O_2 +Fe^{3+}	30.48	47.94	11.21	10.37

XPS provided detailed surface elemental analysis of pyrite and chalcopyrite under various treatments. The survey spectra are presented in Fig. 4IV, while the corresponding relative atomic concentrations are summarized in Tables 1 and 2. The untreated pyrite surfaces were found to contain C, O, S and Fe based on the quantitative analysis in Table 1. Fe^{3+} treatment increased the Fe content by 2.71 at%, confirming Fe^{3+} adsorption, accompanied by a marked enhancement of the Fe 2p peak (Fig. 4IVa), confirming Fe^{3+} adsorption. Sequential H_2O_2/Fe^{3+} treatment yielded an increase of 1.23at% in Fe, though the Fe 2p peak intensity remained intermediate between untreated and Fe^{3+}-only samples. This result indicates that H_2O_2 pre-treatment reduces the Fe^{3+} adsorption capacity on pyrite. C, O, S, Fe and Cu were present on untreated chalcopyrite surfaces. H_2O_2 treatment decreased the Cu content

by 2.86at% while increasing the O content by 3.30at%, with corresponding Cu 2p attenuation and O 1s enhancement (Fig. 4IVc). This oxidation-induced surface dissolution is in agreement with the ICP–OES data. Fe^{3+} treatment alone increased the Fe content by 2.06at% with minor Fe 2p enhancement, suggesting weak adsorption. Sequential H_2O_2/Fe^{3+} treatment substantially increased the O content by 7.02 at%, with a prominent O 1s enhancement. This is attributed to the formation of copper oxides derived from the mineral substrate, along with iron oxides formed from the adsorbed Fe^{3+} species on the surface. Importantly, H_2O_2 treatment consistently reduced the Fe content on both minerals compared to the untreated surfaces, this finding corroborates the ICP–OES findings that H_2O_2 treatment compromises subsequent Fe^{3+} adsorption capacity.

3.2.2. Action mechanism of the combined depressant at the chalcopyrite surface

High-resolution XPS deconvolution of the S 2p, Fe 2p and Cu 2p core levels (Fig. 5) elucidated the chemical state evolution on the chalcopyrite surfaces following H_2O_2, Fe^{3+} and sequential H_2O_2/Fe^{3+} treatments. The S 2p spectrum of the untreated chalcopyrite (Fig. 5I) resolved into four doublets, excluding the energy loss peak at 160.42 eV [35]. The key assignments are as follows: S^{2-} (161.40; 37.38%), S_2^{2-} (162.43; 41.07%), S^0/S_n^{2-} (164.75; 8.60%) and SO_4^{2-} (168.29; 7.14%). The treatment-induced binding energy shifts were minimal (<0.2 eV). H_2O_2 alone depleted S^{2-} to 29.13% while elevating SO_4^{2-} to 12.40%. Conversely, Fe^{3+} alone reduced SO_4^{2-} to 5.50%. Sequential H_2O_2/Fe^{3+} treatment yielded intermediate speciation (S^{2-}:

32.37%; SO_4^{2-}: 10.36%), which is attributed to the attenuation of S oxidation by Fe^{3+} adsorption. Notably, the baseline SO_4^{2-} content of chalcopyrite (7.14%) was significantly lower than that of pyrite (15.47%), with diminished oxidation response to treatments, thereby confirming that chalcopyrite has a higher oxidation resistance than pyrite.

Deconvolution of the Fe 2p spectra (Fig. 5II) reveals significant surface component evolution. The untreated surfaces exhibited three primary iron species: Fe(III)–S (706.8 eV; 42.84%), Fe(III)–O (710.68 eV; 48.15%) and Fe(III)–SO_4 (712.90 eV; 9.01%). Following H_2O_2 oxidation, Fe(III)–S underwent marked depletion to 16.84%, while Fe(III)–O surged to 75.80%, with a concomitant binding energy shift of Fe(III)–SO_4 to 713.22 eV, confirming the preferential conversion of Fe–S to Fe–O bonds. Fe^{3+} treatment alone induced minor chemical shift perturbations (<0.2 eV) but substantially elevated Fe(III)–S (48.65%) while reducing Fe(III)–SO_4 (3.98%), verifying surface chemisorption. Sequential H_2O_2/Fe^{3+} treatment simultaneously diminished both Fe(III)–S (19.57%) and Fe(III)–SO_4 (2.59%); Fe(III)–SO_4 peak was further displaced to 713.29 eV, indicating the synergistic effects of oxidation and adsorption. Complementary Cu 2p analysis (Fig. 5III) demonstrated that H_2O_2 and H_2O_2/Fe^{3+} treatments significantly depleted the Cu(I)–S species while enhancing the Cu(II)–O components, confirming the oxidative transformation. Notably, Fe^{3+} treatment alone also increased the Cu(II)–O proportions via the interfacial iron hydroxide interactions. Collectively, these transformations established

that both Fe^{3+} adsorption and H_2O_2 oxidation primarily drive Fe-centred modifications on the chalcopyrite surfaces, while the Cu components exhibit secondary sensitivity.

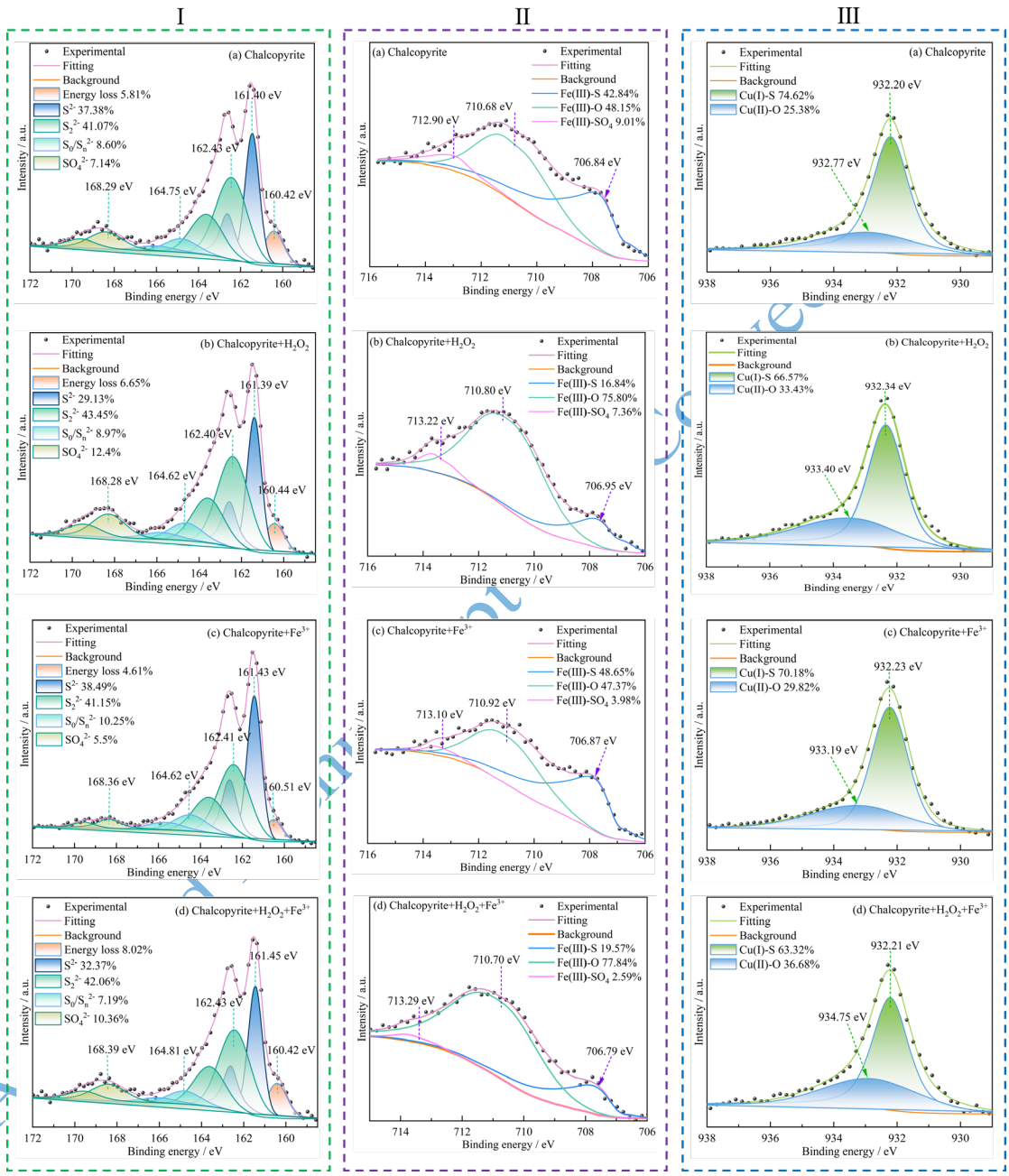

Fig. 5. XPS spectra of S 2p (I), Fe 2p (II) and Cu 2p (III) of chalcopyrite under different conditions.

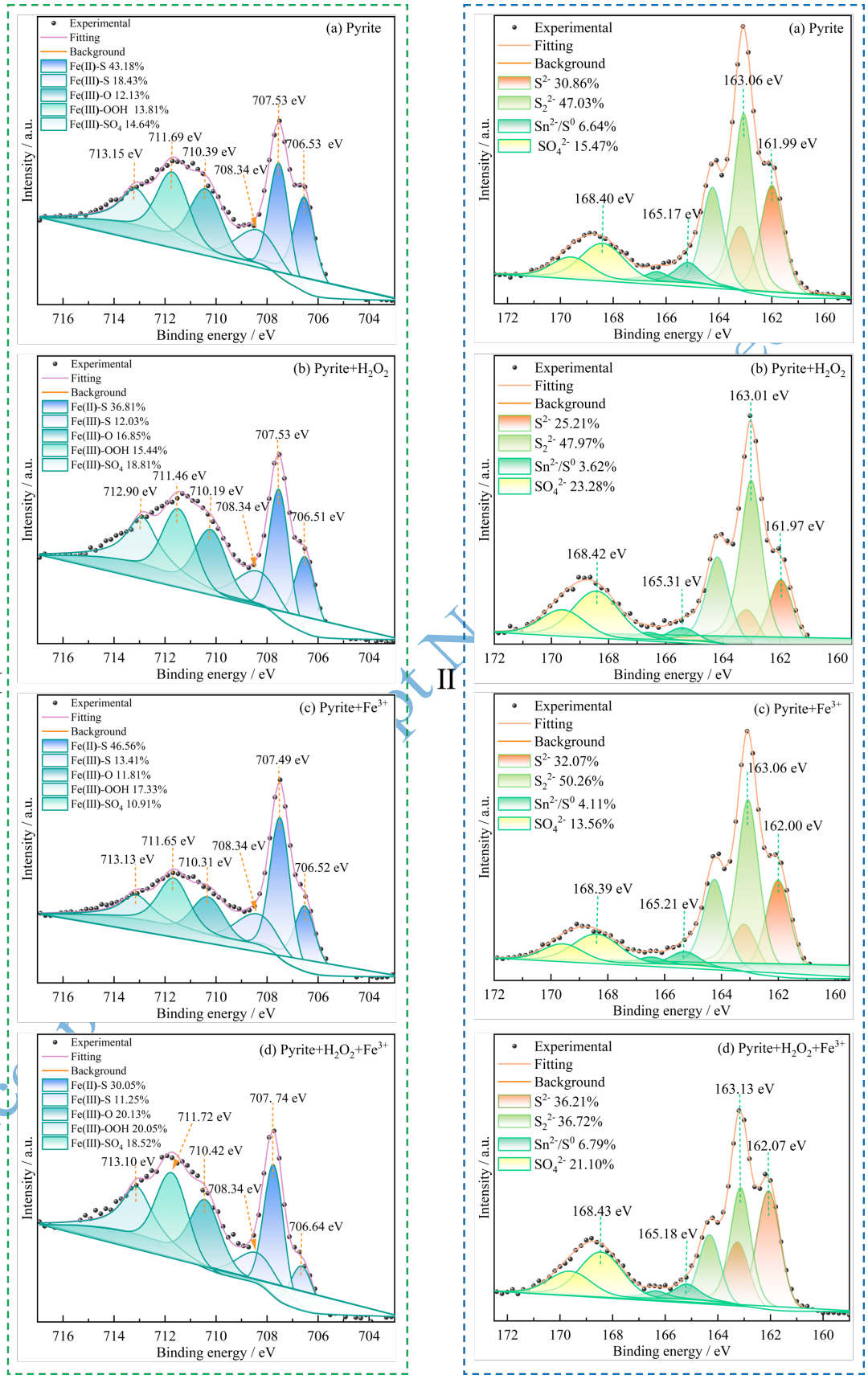

Fig. 6. XPS spectra of Fe 2p (I) and S 2p (II) of pyrite under different conditions.

3.2.3 *Action mechanism of the combined depressant at the pyrite surface*

Studies on chalcopyrite have indicated that H_2O_2 and Fe^{3+} primarily alter the contents of the surficial Fe and S components. Comprehensive high-resolution XPS spectral analysis was performed on pyrite surface elements to establish the mechanistic differences in their actions on this mineral. Fig. 6I(a) shows the deconvoluted Fe 2p XPS spectrum of pyrite, fitted into five characteristic peaks. The peaks at binding energies of 706.53 and 707.53 eV were attributed to the Fe(II)–S species (43.18%), while the peak at 708.34 eV corresponded to the Fe(III)–S species (18.43%). Peaks at 710.39, 711.69 and 713.15 eV were assigned to Fe(III)–O (12.13%), Fe(III)–OH (13.81%) and Fe(III)–SO_4 (14.64%) species, respectively, indicating the tendency of pyrite to undergo surface oxidation under weakly alkaline conditions [25]. Notably, the binding energies of the Fe chemical states across the different treatments exhibited only minor shifts (< 0.2 eV). Following treatment with H_2O_2 alone, the contents of Fe(III)–O, Fe(III)–OH and Fe(III)–SO_4 increased to 16.85%, 15.44% and 18.81%, respectively, confirming the significant enhancement of surface oxidation by H_2O_2 treatment. Conversely, treatment with Fe^{3+} alone resulted in an increase in the Fe(III)–OH content to 17.33% and a decrease in Fe(III)–SO_4 content to 10.91%, suggesting the preferential adsorption of iron ions as Fe(III)–OH species in alkaline environments. Significantly, the combined treatment (H_2O_2 pre-oxidation followed by Fe^{3+} addition) led to a decrease in the contents of Fe(II)–S and Fe(III)–S components to 30.05% and 11.25%, respectively, while simultaneously

increasing the Fe(III)–O, Fe(III)–OH and Fe(III)–SO_4 components to 20.13%, 20.05% and 18.52%, respectively. These results demonstrate that the oxidative action of H_2O_2 and the adsorption of Fe^{3+} collectively promote the accumulation of depressive components, such as Fe(III)–O, Fe(III)–OH and Fe(III)–SO_4, on the pyrite surface, thereby achieving efficient pyrite depression through multi-component adsorption.

Fig. 6II shows the S 2p XPS spectra of the pyrite surfaces under varying treatment conditions, exhibiting a spin-orbit split doublet spacing of 1.18 eV (intensity ratio 2:1) corresponding to the S $2p_{3/2}$ and S $2p_{1/2}$ orbitals, respectively. Deconvolution of the untreated pyrite spectrum revealed four sulphur species: monosulphide S^{2-} (161.99, 30.86%), disulphide S_2^{2-} (163.06, 47.03%), polysulphide Sn^{2-}/S^0 (165.17, 6.64%) and sulphate SO_4^{2-} (168.40, 15.47%). Notably, S^{2-}/S_2^{2-} originate from the pyrite lattice (FeS_2) and confer inherent hydrophobicity, whereas SO_4^{2-}, an oxidation product, imparts strong hydrophilicity [36]. The binding energies of the different chemical states of S across the treatments exhibited minimal shifts (<0.2 eV). Following H_2O_2 treatment, the S^{2-} content decreased to 25.21% while SO_4^{2-} increased to 23.28%, confirming the enhanced oxidation. Conversely, Fe^{3+} treatment alone induced only slight changes: Sn^{2-}/S^0 decreased marginally (6.64% → 4.11%) and SO_4^{2-} reduced to 13.56%, in agreement with the Fe 2p spectral trends. Significantly, the combined treatment (H_2O_2/Fe^{3+}) yielded sulphur species changes analogous to those observed with H_2O_2 treatment alone: S_2^{2-} decreased sharply to 36.72%, and SO_4^{2-} increased to 21.10%, which is slightly lower than that under only

H_2O_2 treatment (23.28%). Collectively, these S 2p results, corroborated by the Fe 2p analysis, demonstrate that H_2O_2 drives pyrite surface hydrophilisation primarily through selective disulphide oxidation and sulphate accumulation, whereas Fe^{3+} adsorption occurs predominantly as hydroxyl compounds.

Fig. 7 and Fig. 8 show the ion fragment images of the pyrite surfaces before and after treatment with H_2O_2 and Fe^{3+}. The total count (TC) and colour brightness reflect the overall ion intensity across the sample surface. Brighter images indicate higher fragment intensities, directly reflecting the adsorption level of the products on the pyrite surface [37]. The ToF-SIMS image analysis revealed that the untreated pyrite surface exhibited prominent S^- and S_2^- signals (Fig. 7), consistent with the characteristic features of sulphides. Concurrently, the SO_4^- signal was weak, confirming that S primarily existed in low-valence states (S^{2-}/S_2^{2-}) under natural conditions. Following H_2O_2 treatment, the signal intensities of these states significantly attenuated, while SO_4^- signal substantially intensified. This observation indicated that the strong oxidising power of H_2O_2 induced extensive oxidation of sulphide sulphur to sulphate (SO_4^{2-}). Minor SO_2^- fragments were detected during this process, suggesting the transient existence of sulphite intermediates. In contrast, treatment with Fe^{3+} alone resulted in limited oxidation of the sulphur species, as evidenced by minimal SO_4^- generation. This implied that Fe^{3+} possessed only a limited oxidising capacity. Conversely, sequential treatment with H_2O_2 followed by Fe^{3+} yielded S^- and S_2^- signals comparable to those observed with H_2O_2 treatment

alone. This result suggested that the transformation of the S species on the pyrite surface was predominantly driven by H_2O_2 oxidation. Subsequently, Fe^{3+} exerted its depressive effect through hydrolytic adsorption onto the oxidised surface.

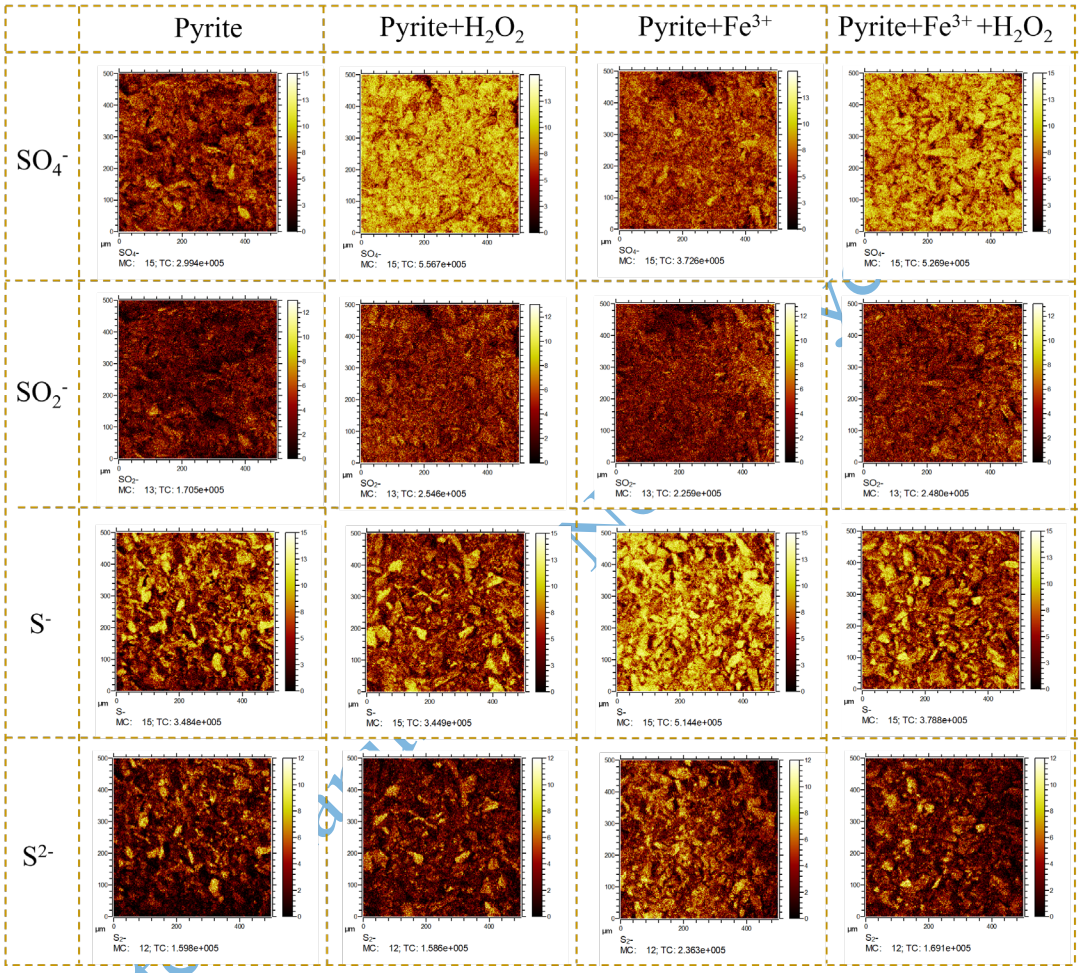

Fig. 7. Surface distribution of S^-, S_2^-, SO_4^- and SO_2^- fragments on pyrite seen in ToF-SIMS images.

Fig. 8 shows the ToF-SIMS images of the OH^-, FeO^{2-}, Fe^+ and Fe_2S^+ ion fragment peaks on the surface of pyrite under different processing conditions. The ToF-SIMS images of the surface of pristine pyrite surface revealed weak OH^- and FeO_2^- signals, reflecting its hydrophobic character. After H_2O_2 treatment, the OH^-

signal intensified significantly due to the generation of hydroxy oxides [25], while the FeO_2^- signal increased owing to Fe^{2+} oxidation to Fe^{3+} and subsequent oxide formation, enhancing the surface hydrophilicity. Fe^{3+} treatment hydrolysed to form hydroxy complexes, substantially increasing OH^- adsorption but yielding minimal FeO_2^-. Combined H_2O_2 pre-treatment and Fe^{3+} addition maximised the OH^- intensity (from synergistic hydroxyl radicals and complexes) with FeO_2^- comparable to that with H_2O_2 treatment alone, achieving peak hydrophilisation. Iron-species analysis revealed dominant Fe^+ and FeS^+ signals in the pristine pyrite, indicating Fe^{2+}–S bonding within the sulphide lattice. H_2O_2 oxidation enhanced Fe^+ intensity (confirming $Fe^{2+} \rightarrow Fe^{3+}$ conversion) and elevated FeS^+ signals (denoting sulphide lattice disruption). Fe^{3+} adsorption similarly increased Fe^+ intensity. After sequential H_2O_2/Fe^{3+} treatment, Fe^+ and FeS^+ signals mirrored those with H_2O_2 treatment alone, confirming the transformation of the hydrophobic sulphide structure into a hydrophilic hydroxy or oxide species.

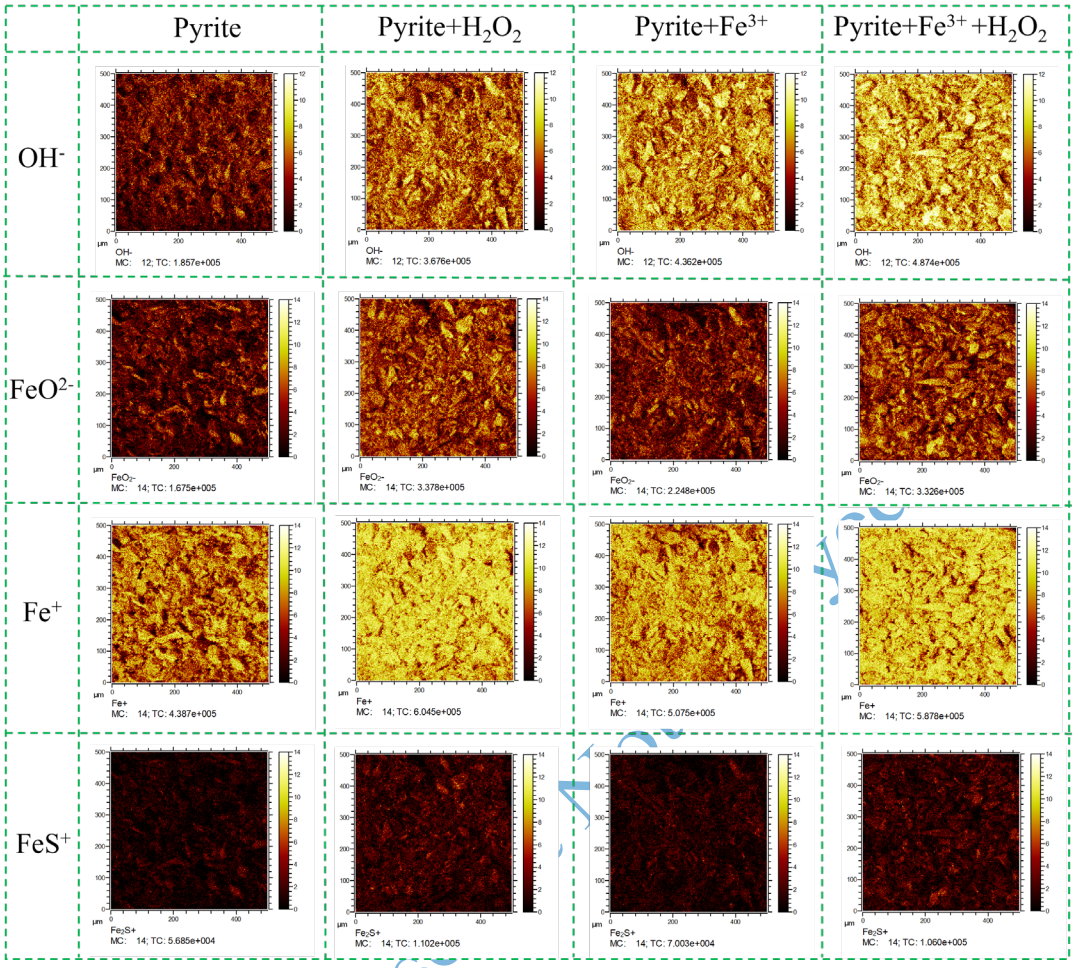

Fig. 8. Surface distribution of OH^-, FeO_2^-, Fe^+ and FeS^+ fragments on pyrite seen in ToF-SIMS images.

The effects of H_2O_2 and Fe^{3+} on pyrite surface morphology were visually elucidated by SEM–EDS analyses. As shown in Fig. 9, the untreated pyrite surfaces were slightly rough with a homogeneous texture and minor mineral debris—this result is correlated with the densely distributed spike-like structures shown in the AFM images. Point scans revealed atomic concentrations of 8.03at% C, 0.42at% O, 48.45at% S and 43.10at% Fe. Following H_2O_2 treatment, the surfaces became smoother with fragmented particulates, while the O content increased to 3.07at%,

confirming the formation of a hydrophilic oxide layer. Fe^{3+}-treated pyrite surfaces displayed densely distributed granular features under high magnification, corresponding to ridge-like protrusions in the AFM images, with the Fe content rising to 47.31%, indicating surface adsorption. Sequential H_2O_2/Fe^{3+} treatment produced flaky particulates, matching clustered protrusions revealed by AFM. However, the Fe content increased only to 45.49%, which is lower than that achieved with Fe^{3+}-only treatment, demonstrating reduced adsorption capacity on the pre-oxidised surfaces. The results of SEM–EDS corroborated AFM observations in visualising surface modifications, while elemental trends showed high consistency with the ICP–OES, XPS and ToF-SIMS analyses.

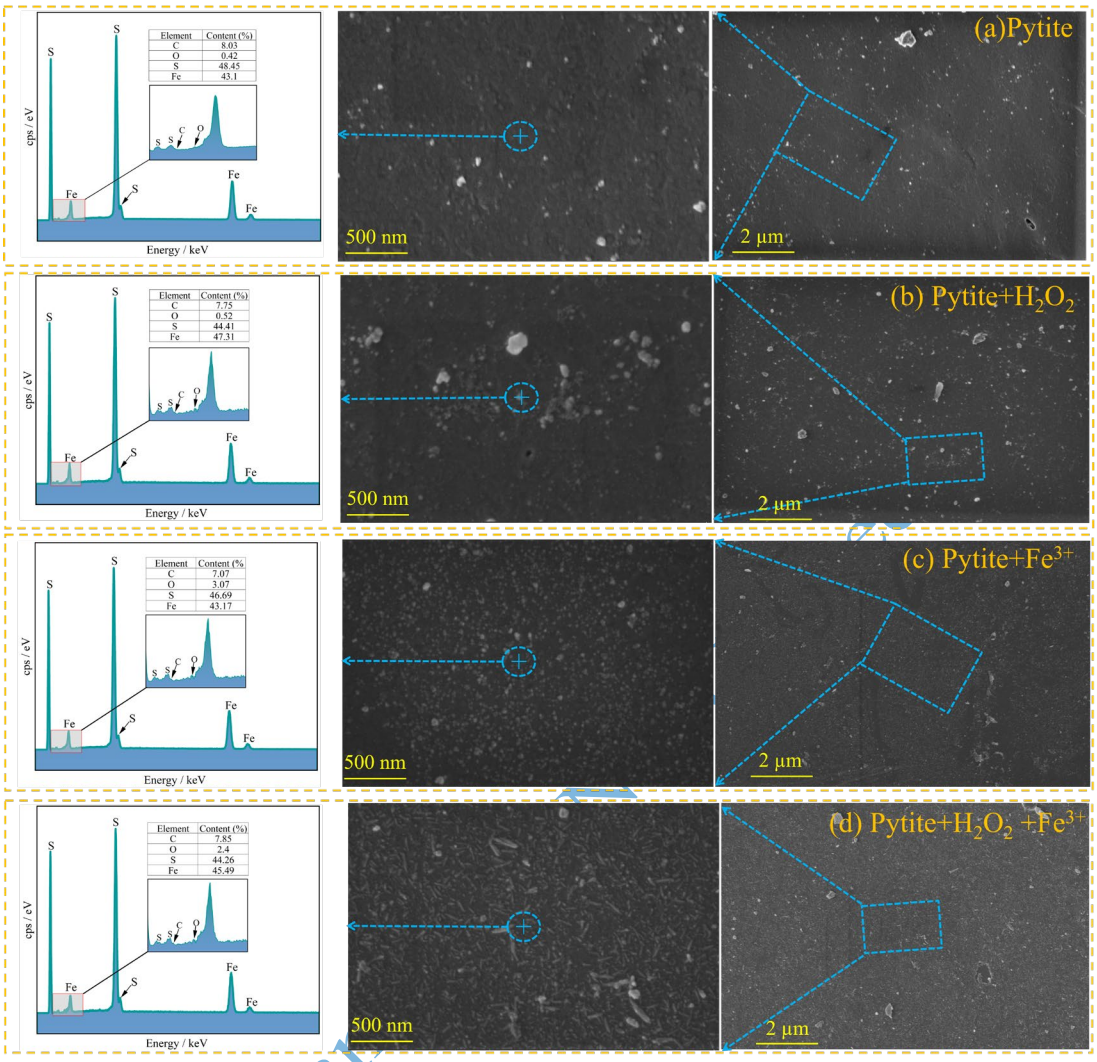

Fig. 9. SEM–EDS analysis of pyrite under different treatments: Morphological and elemental distribution.

3.3. Characterisation of mineral surface hydrophobicity

Fig. 10I illustrates the variations in the surface contact angles of pyrite and chalcopyrite under different treatment conditions. Without any treatment, the contact angles of pyrite and chalcopyrite are 73.71° and 74.09°, respectively, indicating that both minerals possess good natural hydrophobicity, which is consistent with the typical characteristics of sulphide minerals. After the sole action of SEX, the contact

angles of chalcopyrite and pyrite increased to 84.60° and 82.18°, respectively, confirming that SEX was effectively adsorbed on the surfaces of both minerals and enhanced their hydrophobicity. Therefore, selective separation cannot be achieved using SEX alone. When SEX was added after pre-treatment with H_2O_2 or Fe^{3+}, the contact angle of chalcopyrite decreased slightly to 80.58° (H_2O_2) and 79.51° (Fe^{3+}); under identical conditions, the contact angle of pyrite decreased significantly to 67.58° (H_2O_2) and 66.15° (Fe^{3+}), demonstrating the selective depression effect of H_2O_2 and Fe^{3+} on pyrite. After the combined H_2O_2/Fe^{3+} treatment followed by the addition of SEX, the contact angle of chalcopyrite was 78.84°, which was still higher than that of the original ore (74.09°), indicating that the adsorption of SEX was not depressed. The contact angle of pyrite dropped sharply to 58.27°, a decrease of 20.9% compared with that of the original ore (73.71°); this decrease confirmed that its surface hydrophobicity was considerably reduced and that the SEX adsorption pathway was effectively blocked.

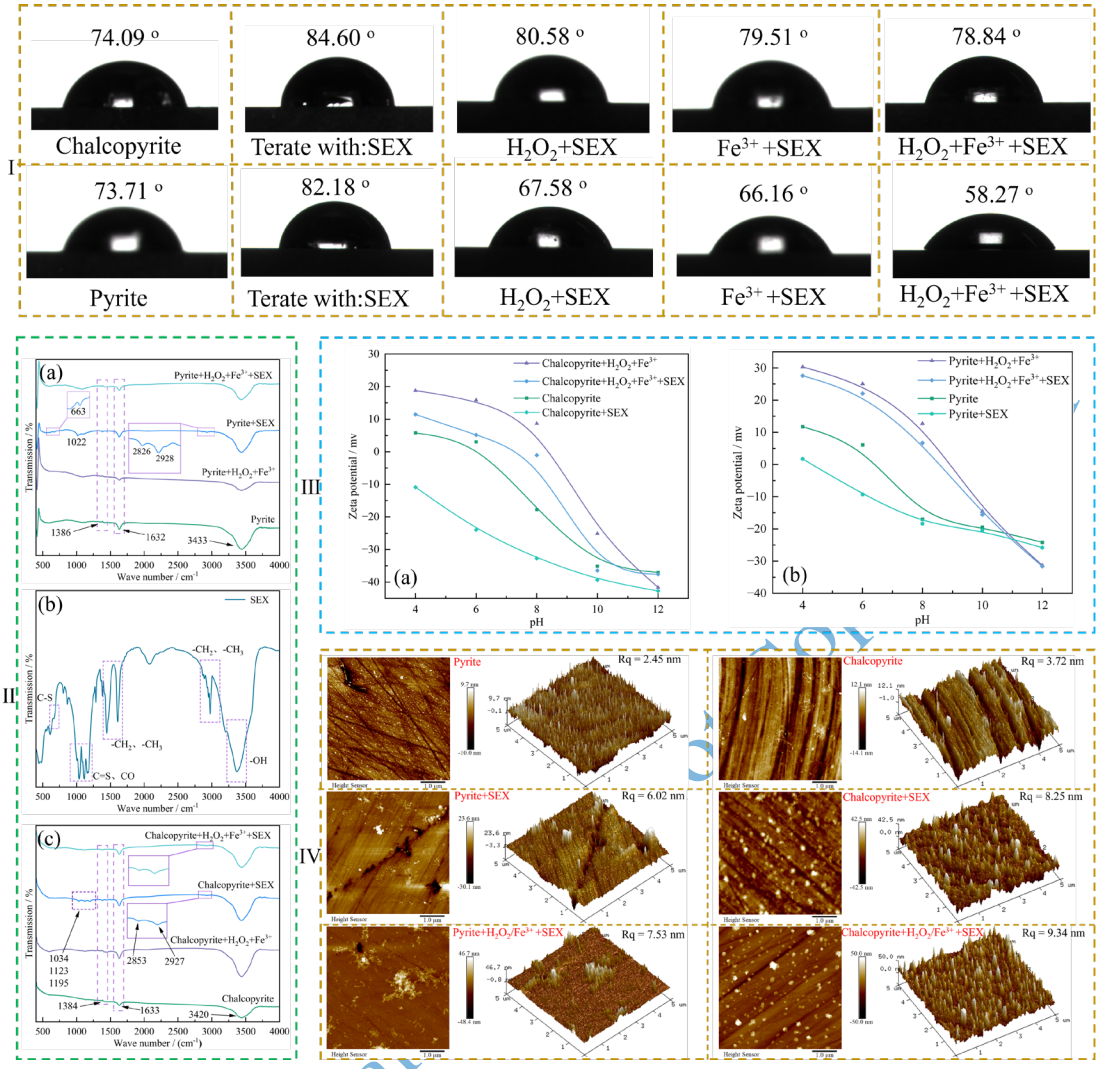

Fig. 10. Surface characterisation of chalcopyrite and pyrite: I. Contact angles under various treatments; II. FTIR spectra of (a) chalcopyrite, (b) SEX and (c) pyrite. III. Zeta potential measurements of (a) chalcopyrite and (b) pyrite. IV. AFM images under different treatments.

Systematic FTIR spectroscopic analysis was conducted to evaluate the influences of Fe^{3+} and H_2O_2 treatments on SEX adsorption characteristics at pyrite and chalcopyrite interfaces. As shown in Fig. 10II(a), the FTIR spectra of pyrite under various reagent conditions reveal characteristic peaks. The spectrum of untreated

pyrite exhibits a stretching vibration peak of free hydroxyl groups (–OH) near 3420 cm^{-1}, while peaks at 1632 and 1386 cm^{-1} are assigned to Fe–S_2 bond stretching vibrations, in agreement with literature [38]. Upon exclusive SEX treatment, the pyrite surface manifests prominent new FTIR spectral signatures: characteristic vibrations emerge at 2928 cm^{-1} (methyl –CH_3 C–H stretch), 2826 cm^{-1} (methylene –CH_2 C–H stretch), 1022 cm^{-1} (C=S stretch), and 663 cm^{-1} (C–S stretch), all attributable to SEX molecular configurations. These features collectively indicate SEX adsorption onto the pyrite surface [39]. Notably, in pyrite samples treated sequentially with H_2O_2/Fe^{3+} followed by SEX, the aforementioned characteristic SEX peaks (2928, 2826, 1022 and 663 cm^{-1}) were absent, confirming that the depressant treatment completely prevented the adsorption of SEX. Fig. 10II(c) shows the FTIR spectra of chalcopyrite. The peak at 3433 cm^{-1} is attributed to –OH stretching, and the peaks at 1632 and 1386 cm^{-1} are assigned to Fe–S_2 vibrations [40]. After SEX treatment, characteristic adsorption peaks appeared in the FTIR spectrum of the chalcopyrite surface: 2853 cm^{-1} (–CH_3), 2927 cm^{-1} (–CH_2) and 1034–1195 cm^{-1} (coupled C=S and C–O vibrations) [41]. Notably, even after pre-treatment with H_2O_2/Fe^{3+}, the characteristic –CH_3 and –CH_2 peaks were detectable upon subsequent SEX addition to the chalcopyrite, indicating that SEX adsorption onto the chalcopyrite surface was not depressed.

The zeta potential, a key parameter characterising electrostatic interactions between colloidal particles, was utilised to effectively evaluate the influence of the

flotation reagents on the surface electrical properties of the minerals [42]. As shown in Fig. 10III, Under reagent-free conditions, both pyrite and chalcopyrite exhibited progressively negative shifts in zeta potential with increasing pH. This behaviour is attributed to the accumulation of negative charges resulting from the adsorption of the enhanced hydroxyl ion (OH^-) onto the mineral surfaces. Following the addition of the collector SEX, the zeta potentials of both minerals underwent a further negative shift. Notably, the magnitude of the decrease was significantly smaller for pyrite than for chalcopyrite, suggesting a higher adsorption density of SEX on the chalcopyrite surface. After the synergistic treatment with H_2O_2/Fe^{3+}, the zeta potentials of both minerals shifted positively. Crucially, this positive shift was more pronounced for pyrite. Following SEX addition, pyrite exhibited a significantly attenuated zeta potential negative shift compared to chalcopyrite. This electrokinetic divergence originates from the hydrophilic barrier generated by prior H_2O_2/Fe^{3+} treatment on pyrite surfaces, selectively suppressing SEX adsorption.

The evolution of the surface microtopography of chalcopyrite and pyrite under different depressant systems (scan size: 2 × 2 μm) was examined by AFM to elucidate differences in reagent adsorption behaviour. The AFM observations presented in Fig. 10IV reveal distinct surface morphologies. The pristine pyrite surface exhibited densely packed spike-like structures (root mean square roughness, *R*q = 2.45 nm), whereas the chalcopyrite surface displayed minor scratches (*R*q = 3.72 nm). Treatment with SEX alone induced the formation of spike-shaped aggregates on the

surfaces of both minerals. Notably, these aggregates were more densely distributed on chalcopyrite (*R*q = 8.25 nm; vertical height range: 0–42.5 nm) than pyrite (*R*q = 6.02 nm; height range: −3.3 to 23.6 nm), confirming the stronger adsorption affinity of chalcopyrite for SEX. Following sequential treatment with H_2O_2/Fe^{3+} and subsequent SEX addition, a pronounced morphological contrast emerged: The chalcopyrite surface retained dense aggregates morphologically similar to those observed after SEX treatment alone (*R*q = 9.34 nm; height range: 0–50.0 nm). Conversely, the spike-like structures on the pyrite surface were significantly disrupted, with only sporadic cluster-like protrusions remaining (*R*q = 7.53 nm; height range: −0.8 to 46.7 nm). This distinct transformation demonstrates the absence of SEX adsorption on the depressed pyrite surface.

3.4. Synergistic depression mechanism of H_2O_2/Fe^{3+}

In a weakly alkaline copper-sulfide flotation system, the selective depression of pyrite is achieved via a synergistic stepwise "oxidation–adsorption" mechanism mediated by H_2O_2/Fe^{3+}. This mechanism originates from intrinsic differences in crystal structure, electronic properties, and surface reactivity between pyrite and chalcopyrite, as schematically shown in Fig.11. As a strong oxidant with specific targeting ability, H_2O_2 preferentially reacts with pyrite, which is characterized by high surface electronic activity and relatively weak Fe–S covalent bonding, and directly attacks Fe–S and S–S bonds on the pyrite surface. Consistent with previous studies [43], this oxidation process converts lattice S^{2-} or S_2^{2-} species into SO_4^{2-}. This

reaction not only disrupts the intrinsic hydrophobic structure of pyrite but also generates sulfur-deficient active sites while releasing trace amounts of Fe^{2+} ions. Under weakly alkaline conditions, these Fe^{2+} ions are oxidized in situ, further forming hydrophilic iron oxyhydroxides such as FeOOH and $Fe(OH)_3$. The overall reaction is expressed as Eq. (2):

$$4FeS_2 + 13H_2O_2 + 2OH^- \rightarrow 2FeOOH + 2Fe(OH)_3 + 8SO_4^{2-} + 8H_2O \quad (2)$$

This oxidation step establishes an activated surface layer facilitating subsequent Fe^{3+} adsorption. In contrast, chalcopyrite exhibits strong hybridization between the Fe 3d and S 3p orbitals, and its Cu–S bonds possess stronger covalency and higher bond energy compared with Fe–S bonds in pyrite. These features result in a more stable surface electronic structure and crystal lattice framework [44-45]. As a result, H_2O_2 induces only minimal oxidation on chalcopyrite, and thus preserves the mineral's surface hydrophobicity. Based on this oxidative pre-treatment, Fe^{3+} further enhances pyrite depression via an adsorption-driven mechanism. Under weakly alkaline conditions, Fe^{3+} hydrolyzes to form hydroxyl-containing species such as $Fe(OH)_2^+$ and $Fe(OH)_3$, as expressed by Eq. (3):

$$Fe^{3+} + 3H_2O \rightarrow Fe(OH)_3 + 3H^+ \quad (3)$$

These hydrophilic species undergo electrostatic attraction to sulfur-deficient sites and hydroxyl groups on the previously oxidized pyrite surface, where they form

Fe–O–S chemical bonds. Consequently, a dense composite hydrophilic film mainly consisting of Fe–SO_4, FeOOH, and $Fe(OH)_3$ is formed, which effectively blocks hydrophobic sites and significantly depresses pyrite flotation.

Conversely, chalcopyrite's stable surface structure offers limited active sites for Fe^{3+} binding. The electronic effect of Cu–S bonds further reduces its affinity for Fe^{3+} adsorption, thus preventing any similar synergistic interaction with H_2O_2. In SEX collector systems, copper-active sites on chalcopyrite preferentially adsorb the collector, thereby preserving high floatability.

Notably, the H_2O_2 concentration must be carefully controlled, as excessive oxidation can damage Cu–S bonds in chalcopyrite and reduce its floatability. The H_2O_2/Fe^{3+} combination overcomes limitations inherent to single-reagent systems: it addresses the poor selectivity of H_2O_2 used alone and boosts the depressing efficiency of Fe^{3+}, as Fe^{3+} alone cannot sufficiently penetrate pyrite's hydrophobic surface unless high dosages are applied. This synergistic approach thus enhances selective pyrite depression while optimizing reagent efficiency.

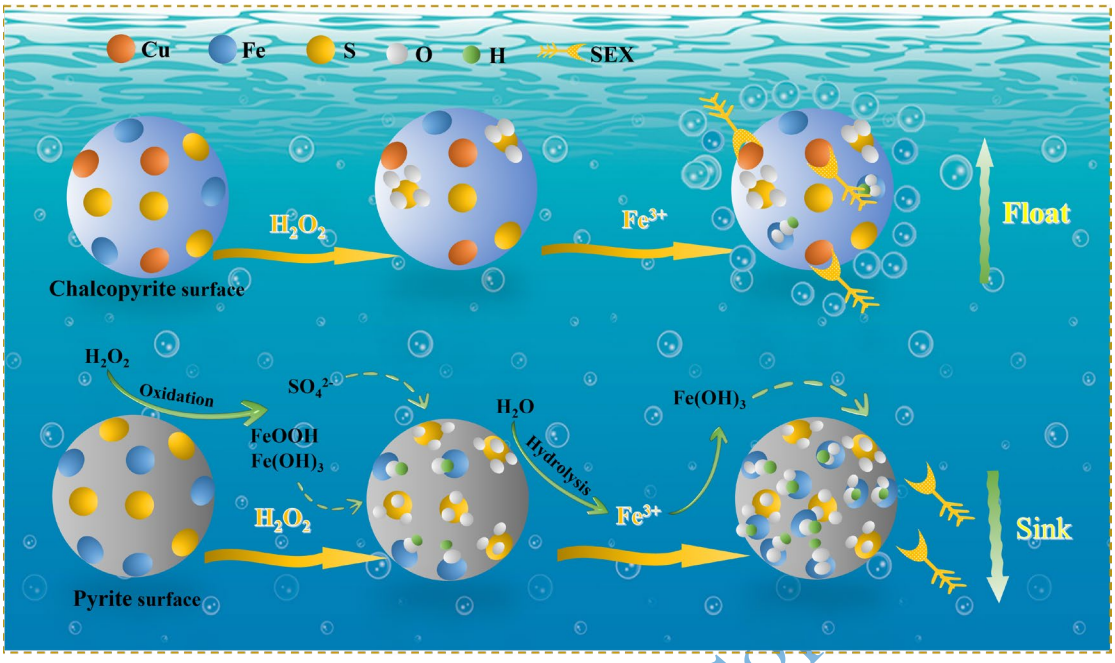

Fig. 11. Synergistic depression mechanism of H_2O_2/Fe^{3+} treatment.

4. Conclusion

This study investigated the impact of a combined depressant system on the flotation separation of chalcopyrite and pyrite, elucidating the progression of surface hydrophobicity transformations and the inherent synergistic depression mechanism. Key findings crystallise as follows:

(1) Flotation performance: Compared with single depressants, the combined H_2O_2/Fe^{3+} system effectively depressed pyrite flotation, enabling efficient pyrite separation from chalcopyrite. The artificial mixed minerals flotation tests yielded a copper concentrate grade of 30.51wt% with a recovery of 88.30%.

(2) Depression mechanism: H_2O_2 selectively oxidises surface S_2^{2-} species on pyrite to SO_4^{2-}, dissolving Fe^{2+} that subsequently form hydrophilic Fe–OOH and Fe–SO_4 species in situ. This generates a S-deficient, reactive surface. The hydrolysed

Fe^{3+} species adsorb onto this pre-oxidised surface, forming a dense, composite hydrophilic layer (Fe–SO_4/ /Fe-OOH/ $Fe(OH)_3$) that completely blocks SEX adsorption.

(3) Hydrophobicity regulation: The synergistic H_2O_2/Fe^{3+} pre-treatment selectively and efficiently suppresses SEX adsorption on pyrite, considerably disrupting its surface hydrophobicity. In contrast, the treatment results in limited depression of chalcopyrite. This distinct response enables the selective flotation separation of chalcopyrite from pyrite.

Conflict of Interest

The authors have no competing interests to declare that are relevant to the content of this article.

Acknowledgments

This work was supported by Yunnan Science and Technology Leading Talent Project (Grant No. 202305AB350005) and Central Guidance Local Scientific and Technological Development Funds (Grant No. 202407AB110022).

Data availability

Data will be made available on request.

Reference

[1] T. Chen, R.Q. Liu, W.C. Dong, M. Wei, and W. Sun, Differential adsorption of

gum Arabic as an eco-friendly depressant for the selective flotation of chalcopyrite from molybdenite, Int. J. Miner. Metall. Mater., 32(2025), No. 8, p. 1838-1847.

[2] M. Levie, H.S. Park, S. Kang, and H. Kim, Separation of chalcopyrite from a siliceous copper ore using polyethylene oxide as a depressant: An experimental study complimented by theoretical investigation, Miner. Eng., 204(2023), p. 108445.

[3] M. Levie, G.P. Khanal, Insights into the separation of chalcopyrite from pyrite in Mg and Ca using gum acacia, xanthomonas campestris and guar gum: An experimental study validated by theoretical investigations, Miner. Eng., 218(2024), art. No. 109047.

[4] S.L. Chen, Z.H. Shen, S.M. Wen, G. Han, and Q.C. Feng, Effect of D-arginine as a novel depressant on the flotation separation of chalcopyrite from pyrite at low alkalinity, Appl. Surf. Sci., 682(2025), art. No. 161657.

[5] Z.H. Shen, S.M. Wen, G. Han, Y.W. Zhou, X. Bai, and Q.C. Feng, Selective depression mechanism of locust bean gum in the flotation separation of chalcopyrite from pyrite in a low-alkalinity media, Miner. Eng., 170(2021), art. No. 107044.

[6] G. Han, S.M. Wen, H. Wang, and Q.C. Feng, Interaction mechanism of tannic acid with pyrite surfaces and its response to flotation separation of chalcopyrite from pyrite in a low-alkaline medium, J. Mater. Res. Technol., 9(2020), No. 3, p. 4421.

[7] G. Han, S.M. Wen, H. Wang, Q.C. Feng, and X. Bai, Pyrogallic acid as depressant for flotation separation of pyrite from chalcopyrite under low-alkalinity conditions, Sep. Purif. Technol., 267(2021), art. No. 118670.

[8] S.M. Wen, Y.C. Miao, Y.Y. Tang, Z.Y. Song, and Q.C. Feng, Theoretical and experimental study on high-entropy flotation of micro-fine cassiterite, Int. J. Min. Sci. Technol., 35(2025), No. 1, p. 19.

[9] Z.H. Wang, G. Han, and Q.C. Feng, Selective flotation of galena and sphalerite using N-(phosphonomethyl) iminodiacetic acid as an eco-friendly depressant, Green Smart Min. Eng., 1(2024), No. 1, p. 96.

[10] T. Chen, R.Q. Liu, W.C. Dong, M. Wei, and W. Sun, Interfacial differentiation of a high-performance collector adsorption enabling selective flotation separation of chalcopyrite from pyrite, Miner. Eng., 231(2025), art. No. 109478.

[11] Y.Y. Tang, W.H. Yang, S.L. Chen, Z.H. Shen, Q.C. Feng, and Q. Zhang, A green and biodegradable depressant for efficient flotation separation of smithsonite from calcite, Sep. Purif. Technol., 380(2026), art. No. 135562.

[12] G.K. Ye, Y. Miao, D.Z. Liu, H. Zheng, G.F. Zhang, and W. Yang, New insights into environmentally friendly inhibitors for the flotation separation of chalcopyrite and pyrite: Experimental and theoretical explorations, Colloids Surf. A, 722(2025), art. No. 137234.

[13] Q.Z. Yuan, M.Y. Wang, C.L. Shi, J. Fang, X.H. Qiu, and T.S. Qiu, Activation flotation and activating mechanism of cyanide-depressed pyrite using sodium persulfate and ferrous sulfate, Miner. Eng., 224(2025), art. No. 109206.

[14] M.M. Liu, C. Cheng, L.Y. Wang, Z.H. Qiu, S. Liu, W. Chen, and G.Y. Liu, The green separation of sphalerite from pyrite: Triazine-dithione collector and its flotation mechanism, Colloids Surf. A, 718(2025), art. No. 136947.

[15] L.X. Zhao, K.Y. Li, S.T. Matkarimov, C. Liu, S.X. Bao, and S.Y. Yang, Mechanical activation improves green depressant starch for the flotation separation of pyrite from chalcopyrite via molecular structure optimization, J. Mol. Liq., 424(2025), art. No. 127122.

[16] J.J. Zhong, Q.C. Zhang, S.B. Xing, W. Sun, H.H. Tang, L.M. Zhang, F. Jiang, and Y.J. Luo, A new attempt for low-alkalinity flotation separation of chalcopyrite/molybdenite from pyrite using nonpolar collectors, J. Mol. Liq., 422(2025), art. No. 126898.

[17] C. Cheng, M.M. Liu, Z.H. Qiu, S. Liu, W. Chen, and G.Y. Liu, The low-alkaline

separation of chalcopyrite from pyrite: Triazine-thiol collectors and their flotation mechanism, Appl. Surf. Sci., 690(2025), art. No. 162648.

[18] Y.J. Xian, S.M. Wen, S.J. Bai, and C.Y. Chen, Metal ions released from fluid inclusions of quartz associated with sulfides, Miner. Eng., 50-51(2013), p. 1.

[19] Q. Zhang, S.M. Wen, Z.Y. Song, Y.Y. Tang, and Q.C. Feng, Advances in zinc oxide mineral flotation: Fundamentals, practices and perspectives, Miner. Eng., 233(2025), art. No. 109621.

[20] Y.B. Sun, S.M. Wen, Q.C. Feng, Y.Y. Tang, Y.C. Miao, X. Wang, and Z.H. Shen, Efficient flotation of sodium lauroyl sarcosinate on Pb^{2+}-modified rutile surface: experimental study and DFT calculation, Appl. Surf. Sci., 702(2025), art. No. 163330.

[21] P.X. Li, G. Zhang, W.J. Zhao, G. Han, and Q.C. Feng, Interaction mechanism of Fe^{3+} with smithsonite surfaces and its response to flotation performance, Sep. Purif. Technol., 291(2022), art. No. 121001.

[22] L. Yu, Q.J. Liu, S.M. Li, J.S. Deng, B. Luo, and H. Lai, Depression mechanism involving Fe^{3+} during arsenopyrite flotation, Sep. Purif. Technol., 222(2019), p. 109.

[23] J.F. He, H. Chen, M.M. Zhang, L.H. Chen, Q.Y. Yao, Y.P. Dai, L.T. Zhu, and C.G. Liu, Combined inhibitors of Fe^{3+}, Cu^{2+} or Al^{3+} and sodium silicate on the flotation of fluorite and quartz, Colloids Surf. A, 643(2022), art. No. 128702.

[24] J.S. Dong, Q.J. Liu, L. Yu, and S.H. Subhonqulov, The interaction mechanism of Fe^{3+} and NH_4^+ on chalcopyrite surface and its response to flotation separation of chalcopyrite from arsenopyrite, Sep. Purif. Technol., 256(2021), art. No. 117778.

[25] Z. Ding, M.J. Chen, J.Q. Yuan, A.M. Yu, H.X. Dai, and S.J. Bai, Fenton oxidation modification mechanism of pyrite and its response to Cu–S flotation separation: Experiment, DFT, XPS and ToF-SIMS studies, Appl. Surf. Sci., 652(2024), art. No. 159305.

[26] M.C. Biesinger, B.P. Payne, A.P. Grosvenor, L.W.M. Lau, A.R. Gerson, and

R.St.C. Smart, Resolving surface chemical states in XPS analysis of first row transition metals, oxides and hydroxides: Cr, Mn, Fe, Co and Ni, Appl. Surf. Sci., 257(2011), No. 7, p. 2717-2730.

[27] Z. Ding, Y.X. Bi, J. Li, J.Q. Yuan, H.X. Dai, and S.J. Bai, Flotation separation of chalcopyrite and pyrite via Fenton oxidation modification in a low alkaline acid mine drainage (AMD) system, Miner. Eng., 187(2022), art. No. 107818.

[28] S.L. Chen, Z.H. Shen, Z.Y. Song, G. Han, and Q.C. Feng, Selective flotation separation of chalcopyrite from pyrite using 2-phenylimidazoline as a collector: Flotation performance and surface adsorption mechanism, J. Environ. Chem. Eng., 13(2025), No. 3, art. No. 116200.

[29] K. Feng, J. Cao, D.D. Wu, J.A. Li, Q. Zuo, and S.J. Bai, Selective passivation of arsenopyrite surface using a novel eco-friendly oxidant, sodium percarbonate, for Cu–As flotation separation, Chem. Eng. J., 515(2025), art. No. 163664.

[30] J.Q. Yuan, Z. Ding, Y.X. Bi, J. Li, S.M. Wen, and S.J. Bai, Acid mine drainage activation mechanism on lime-depressed pyrite flotation from copper sulfide ore, Trans. Nonferrous Met. Soc. China, 34(2024), No. 9, p. 2987.

[31] Z. Lei, H. Zhang, H. Tang, Y.C. Luo, and P.F. Xu, Selective flotation separation of chalcopyrite from talc utilizing a novel carboxyl copolymer depressant, J. Environ. Chem. Eng., 13(2025), No. 3, art. No. 117093.

[32] G.K. Parker, R. Woods, and G.A. Hope, Raman investigation of chalcopyrite oxidation, Colloids Surf. A, 318(2008), No. 1-3, p. 160.

[33] H.D. Li, C.R. Yang, W.Q. Qin, Z.Y. Tian, C.F. Wu, Q. Wei, and F. Jiao, In situ Raman investigation of dissolved constituent and its evolution in pulp during Zn–S selective flotation with two-step pulp regulation, Miner. Eng., 192(2023), art. No. 107994.

[34] D. Neff, L. Bellot-Gurlet, P. Dillmann, S. Reguer, and L. Legrand, Raman spectroscopy of corrosions in iron archaeological artefacts, J. Raman Spectrosc., 37(2006), No. 10, p. 1228.

[35] Y.L. Mikhlin, A.A. Karacharov, and M.N. Likhatski, Effect of adsorption of butyl xanthate on galena, PbS, and HOPG surfaces as studied by atomic force microscopy and spectroscopy and XPS, Int. J. Miner. Process., 144(2015), p. 81.

[36] C.L. Li, S.J. Bai, Z. Ding, P. Yu, and S.M. Wen, Visual MINTEQ model, ToF–SIMS, and XPS study of smithsonite surface sulfidation behavior: Zinc sulfide precipitation adsorption, J. Taiwan Inst. Chem. Eng., 96(2019), p. 53.

[37] Q.C. Feng, Y.C. Zhang, G. Zhang, G. Han, and W.J. Zhao, Innovative scheme for hemimorphite flotation: Synergistic activation performance and mechanism, Int. J. Miner. Metall. Mater., 32(2025), No. 6, p. 1297-1308.

[38] T. Chen, R.Q. Liu, M. Wei, J.L. Sun, and W. Sun, Artemisia sphaerocephala krasch gum for selective pyrite depression in chalcopyrite flotation: Interfacial reaction and application research, Appl. Surf. Sci., 709(2025), art. No. 163851.

[39] X. Rao, C.Y. Zhang, W. Sun, J.H. Chen, and H.L. Zhang, Malachite sulfidation flotation mechanism: Cu–S co-deposition insights, Sep. Purif. Technol., 364(2025), No. Part 3, art. No. 132476.

[40] T. Chen, R.Q. Liu, W.C. Dong, M. Wei, and W. Sun, Interfacial differentiation of a high-performance collector adsorption enabling selective flotation separation of chalcopyrite from pyrite, Miner. Eng., 231(2025), art. No. 109478.

[41] Q. Zhang, Y.J. Wang, Q.C. Feng, S.M. Wen, Y.W. Zhou, W.L. Nie, and J.B. Liu, Identification of sulfidization products formed on azurite surfaces and its correlations with xanthate adsorption and flotation, Appl. Surf. Sci., 511(2020), art. No. 145594.

[42] J.Q. Yuan, X. Gong, H.Y. Lu, H. Lai, S.M. Wen, S.J. Bai, D.D. Wu, and Y.X. Zheng, Selective flotation separation of ilmenite from fine-grained titanaugite utilizing environmentally friendly depressant sodium alginate: Experimental and mechanistic study, Appl. Surf. Sci., 708(2025), art. No. 163705.

[43] Y.L. Jin, H.Y. Xie, L.Y. Dong, P.L. Shen, D.W. Liu, and L. Jin, A green depressant used for the efficient flotation separation of chalcopyrite and

arsenopyrite: Experiment and theoretical study, Colloids Surf. A, 725(2025), No. Part 1, art. No. 137590.

[44] G.K. Ye, Y. Miao, D.Z. Liu, H. Zheng, G.F. Zhang, and W. Yang, New insights into environmentally friendly inhibitors for the flotation separation of chalcopyrite and pyrite: Experimental and theoretical explorations, Colloids Surf. A, 722(2025), art. No. 137234.

[45] L. Glasser, Chalcopyrite thermochemistry: The simple salt approximation together with quantum DFT methods, J. Chem. Thermodyn., 186(2023), art. No. 107126.